

Article

Quantum Study of the Optical Conductivity of Composite Films Formed by Bilayer Graphene and Single-Walled Carbon Nanotubes under Axial Stretching

Michael M. Slepchenkov , Pavel V. Barkov and Olga E. Glukhova * 

Department of Radioengineering and Electrodynamics, Institute of Physics, Saratov State University, Astrakhanskaya street 83, 410012 Saratov, Russia

* Correspondence: glukhovae@info.sgu.ru; Tel.: +7-8452-514562

Abstract: In this article, quantum methods are used to study the optical properties of composite films formed by AB-stacked bilayer graphene and chiral single-walled carbon nanotubes (SWCNT) (12, 6) with a diameter of 1.2 nm. The analysis of optical properties is carried out on the basis of the results of calculating the diagonal elements of complex optical conductivity tensor in the wavelength range of 0.2–2 μm . Two cases of electromagnetic radiation polarization are considered: along the X axis (along the graphene bilayer) and along the Y axis (along the nanotube axis). The calculations are performed for three topological models (V1, V2, V3) of composite films, which differ in the width of the graphene bilayer and in the value of the shift between graphene layers. It is found that in the case of polarization along the X axis, the profile of the real part of optical conductivity in the region of extremal and middle UV radiation is determined by SWCNT (12, 6), and in the region of near UV and visible radiations, it is determined by bilayer graphene. In the case of polarization along the Y axis, the profile of the real part of optical conductivity in the region of extremal, near UV, and visible radiation is determined by SWCNT (12, 6), and in the region of the mid-UV range, it is determined by bilayer graphene. Regularities in the change in the profile of the surface optical conductivity of bilayer graphene-SWCNT (12,6) composite films under the action of stretching deformation along the Y axis are revealed. For models V1 (width of the graphene nanoribbon is 0.5 nm, the shift between layers is 0.48 nm) and V2 (width of the graphene nanoribbon is 0.71 nm, the shift between layers is 0.27 nm), the shift of the conductivity peaks in the region of extreme UV radiation along the wavelength to the right is shown. For the model V3 (width of the graphene nanoribbon is 0.92 nm, the shift between layers is 0.06 nm), the shift of the conductivity peaks to the right along the wavelength is observed not only in the region of extreme UV radiation, but also in the region of visible radiation. It is assumed that graphene-SWCNT (12,6) composite films with island topology are promising materials for photodetectors in the UV-visible and near-IR ranges.



Citation: Slepchenkov, M.M.; Barkov, P.V.; Glukhova, O.E. Quantum Study of the Optical Conductivity of Composite Films Formed by Bilayer Graphene and Single-Walled Carbon Nanotubes under Axial Stretching. *Quantum Rep.* **2023**, *5*, 253–266. <https://doi.org/10.3390/quantum5010017>

Academic Editors: Jorge Garza, Rubicelia Vargas and Andrei L. Tchougréeff

Received: 31 December 2022

Revised: 26 February 2023

Accepted: 2 March 2023

Published: 6 March 2023

Keywords: optical conductivity; density-functional tight-binding method; hybrid carbon films; bilayer graphene; single-walled carbon nanotubes; axial stretching; Kubo-Greenwood formula

1. Introduction

Composite nanostructures obtained by combining two-dimensional (2D) graphene and one-dimensional (1D) carbon nanotubes (CNTs) have been widely discussed in scientific publications over the past ten years [1–10]. Thanks to the capabilities of modern synthesis technologies, graphene-CNT composite materials with different topologies have been obtained in a real experiment [11]. There are three generally accepted topological types of graphene-CNT composite structures: (1) composites with horizontally oriented CNTs relative to the graphene sheet; (2) composites with vertically oriented CNTs relative to the graphene sheet; (3) composites with CNTs wrapped in graphene sheets [12]. Graphene-CNT composites of the first topological type are the most common objects of scientific



Copyright: © 2023 by the authors. Licensee MDPI, Basel, Switzerland. This article is an open access article distributed under the terms and conditions of the Creative Commons Attribution (CC BY) license (<https://creativecommons.org/licenses/by/4.0/>).

research and applied development. For the synthesis of graphene-CNT composites, both single-walled CNTs (SWCNTs) and multi-walled CNTs (MWCNTs) are used [10,11,13–15]. To create electronic devices, the choice of SWCNTs is preferable due to their higher specific surface area, lower defect density, and tuned electronic characteristics in accordance with the chirality of nanotubes [16]. Synthesized ultrathin graphene-SWCNT composites, in which nanotubes and graphene are bonded by van der Waals forces [17,18] or covalently [19–21], demonstrate an increase in mechanical, electrical, and optical properties compared to individual carbon materials. The range of potential applications of graphene-SWCNT composite structures is quite wide: they can be used as flexible and transparent electrodes for batteries [22], diodes [23], transistors [24], sensors [25], as well as in vacuum electronic devices [26]. The unique optoelectronic properties of graphene-SWCNT composites make them promising materials for creating photodetecting devices and optical sensors [14,27–29].

For the efficient use of graphene-SWCNT composites in nano- and optoelectronic devices, it is important to be able to tune their properties. This is facilitated by understanding the regularities of physical processes at the atomic level, including an understanding of how topological features affect the physical properties of graphene-SWCNT composites. This possibility is provided by computer simulation methods. For example, they have been used to reveal the mechanisms of thermal and electrical conduction in graphene-SWCNT composites [30,31]. Using nonequilibrium molecular dynamics, it has been shown that inelastic phonon scattering plays a significant role in the thermal boundary conductivity of composite structures based on graphene nanoribbons and horizontally oriented SWCNTs [30]. Using the DFT and nonequilibrium Green's function methods, it was found that the electrical conductivity of a graphene-nanotube composite structure [31], with one armchair and two zigzag SWCNTs, increases due to the appearance of additional electronic states at the Fermi level caused by graphene flakes. The density-functional tight-binding (DFTB) modeling of graphene-SWCNT (8,8) and graphene-SWCNT (16,0) composites revealed the determining role of structural deformations in the appearance of noticeable shifts in the Raman scattering frequencies of SWCNTs and graphene in the composite structure [32]. Regularities in the transport properties of graphene-SWCNT structures were revealed depending on the type of CNT conductivity [33], the distance between CNTs [34], and the distance between graphene and CNTs [35], the width and shape of the graphene nanoribbon edge [36]. Wei and Zhang investigated the geometric features and electronic properties of hybrid structures formed by the (8,0) CNT and graphene, having different topology defects. Having considered nine different variants of seamless (8,0) CNT-graphene connection and having carried out the Mulliken population analysis for them, the authors found that the lost amount of the charge on the atoms of the tube were higher than that of graphene atoms. It was predicted that the Mulliken charge transfer occurs between atoms at the junction between the graphene and nanotube, which means that there are weak ionic bonds between these atoms in addition to strong covalent bonds [37].

At the same time, the influence of topology on the optical properties of graphene-SWCNT composite structures remains poorly understood. In addition, in the articles mentioned above, calculations were performed for topological models of graphene-SWCNT composites with non-chiral SWCNTs, while most synthesized SWCNTs are chiral nanotubes with a diameter of ~1.2 nm [38]. In this paper, we conduct a quantum study of the optical properties of graphene-SWCNT composite films with island topology, which are affected by axial tensile strain.

2. Materials and Methods

Calculations of the atomic configuration of the studied graphene-SWCNT (12,6) composite structures were carried out within the framework of the self-consistent-charge-DFTB method (SCC-DFTB), implemented in the DFTB+ 20.2 software package [39]. The SCC-DFTB model uses the valence approximation, according to which the largest contribution to the total energy is made by valence orbitals described in terms of the basis of Slater-type

orbitals. The tight-binding approximation is incorporated into the DFT model using perturbation theory. The distribution of the electron charge density over atoms and, accordingly, the excess/insufficient charge on atoms, is determined from the analysis of populations according to the Mulliken scheme [40].

The choice of the SCC-DFTB method for our studies is explained by the following reasons. The DFTB quantum method was first presented as an effective tool for describing carbon systems in 1995. Using the example of carbon clusters, fullerene molecules, hydrocarbon compounds, and solid-state modifications of carbon, the reliability of the DFTB method in calculating the geometric and energy characteristics of carbon materials was proved in comparison with experimental data and ab initio calculation data [41,42]. More recently, the accuracy of the DFTB method has been further improved by adding SCC corrections to account for charge transfer due to interatomic interactions [43]. At present, the SCC-DFTB method is widely used to study the structural features of graphene and carbon nanotubes, as well as composite materials based on them. In particular, this method was previously used to calculate the energy of defect formation in the graphene atomic network [44], to predict the formation mechanism of connections between vertical carbon nanotubes and graphene sheets [45], and to determine the topological and energy conditions for obtaining nanotubes from two parallel graphene nanoribbons [46]. In recent years, some scientific papers have been devoted to the SCC-DFTB study of the structural, vibrational, electronic, and transport properties of graphene-nanotube junctions [32–34,37]. In 2022, Jung et al. conducted a DFT and DFTB study of the mechanical deformation and fracture of pristine graphene. Comparison of the results of DFT and DFTB calculations under various loading conditions showed good agreement in terms of deformation and strain stress behaviors [47]. Previously, the authors of this article successfully applied the SCC-DFTB method to study the atomic and electronic structure of various graphene-nanotube hybrid structures [48–50].

The optical properties of graphene-SWCNT composite structures were studied within the framework of the theory of linear response of an electron population to an applied external electromagnetic field [51]. According to this approach, the complex dynamic electrical conductivity is defined as the coefficient $\sigma(\omega) = \sigma_1(\omega) + i\sigma_2(\omega)$ between the Fourier components of the perturbing external field E_ω and the electric current density j_ω of the frequency ω ($j_\omega = \sigma(\omega) \cdot E_\omega$).

In order to calculate the elements of the complex optical conductivity tensor $\sigma_{\alpha\beta}$, we used the Kubo-Greenwood formula [52], which can be written as:

$$\sigma_{\alpha\beta}(\omega) = \frac{2e^2}{im_e^2 S_{cell}} \frac{1}{N_{\vec{k}}} \sum_{\vec{k} \in BZ} \sum_{m,n} \frac{\hat{P}_\alpha^{nm}(\vec{k}) \cdot \hat{P}_\beta^{mn}(\vec{k})}{E_n(\vec{k}) - E_m(\vec{k}) + i\eta} \times \frac{f_\beta[E_n(\vec{k}) - \mu] - f_\beta[E_m(\vec{k}) - \mu]}{E_n(\vec{k}) - E_m(\vec{k})} \quad (1)$$

where m_e and e are the free-electron mass and electron charge; \hbar is the reduced Planck constant; S_{cell} is the area of the supercell of graphene-SWCNT composite structure; $N_{\vec{k}}$ is the number of k -points needed to sample the Brillouin zone (BZ); \hat{P}_α^{nm} and \hat{P}_β^{mn} are the matrix elements corresponding to the α - and β -components of the momentum operator vector; $E_n(\vec{k})$ and $E_m(\vec{k})$ are the subband energy for valence band and conductivity band; $f_\beta(x) = 1/(1 + \exp[\beta(x - \mu)])$ is the Fermi-Dirac function of the chemical potential μ and the inverse of thermal energy $\beta = 1/k_B T$. The spin degeneracy is already considered in the above equations by factor 2, η is a phenomenological parameter characterizing electron scattering processes. In order to calculate the elements of the impulse matrix $\hat{P}_\alpha^{nm}(\vec{k})$, we used known substitution $P(\vec{k}) \rightarrow (m_e/\hbar)\nabla_{\vec{k}}\hat{H}(\vec{k})$, where $\hat{H}(\vec{k})$ is the Hamiltonian. A detailed description for the calculation of the matrix elements of the momentum operator is given in the work [53]. The Hamiltonian was constructed using the SCC-DFTB method.

The derivation of Equation (1) is based on a microscopic consideration of electron transitions under the action of an electric field in the first order of time perturbation theory.

The starting point for its derivation is the Liouville–von Neumann equation for the density matrix. The independent electron approximation and the adiabatic inclusion (infinitely slow) of a perturbing external electric field are used. A detailed description of the derivation of the Kubo–Greenwood formula is detailed in [51,54].

3. Results and Discussion

This study is carried out for three topological models of graphene-SWCNT composite films. They are composite structures formed by AB-stacked bilayer graphene and horizontally oriented chiral SWCNTs (12,6) with a diameter of ~ 1.2 nm. Bilayer graphene is located above the nanotube in a supercell, forming the so-called “islands” of increased carbon density in the composite structure, which correspond to the experimental data [4]. These models were selected based on the results of our previous study [50]. It was shown that the considered topological models are thermodynamically stable at room temperature [50]. The thermodynamic stability was estimated from the binding energy E_b , which was separately calculated as the difference between the energy of the graphene/SWCNT hybrid structure and the energy of bilayer graphene and SWCNT (12,6). The calculated value of E_b were negative for all considered atomic models; therefore, the resulting atomic configurations of supercells are energetically favorable. Furthermore, these models have demonstrated promising electronic and transport properties [50].

The supercell of each model included fragments of bilayer graphene in the form of zigzag nanoribbons. The width of the graphene nanoribbon was 0.5 nm (two hexagons) for model V1, 0.71 nm (three hexagons) for model V2, and 0.92 nm (four hexagons) for model V3. The graphene layers were shifted relative to each other in the direction of the armchair edge (along the Y axis): the shift value was 0.48 nm for model V1, 0.27 nm for model V2, and 0.06 nm for model V3. Translation vectors of supercells of topological models: $L_x = 1.71$ nm and $L_y = 1.13$ nm for model V1; $L_x = 1.70$ nm and $L_y = 1.11$ nm for model V2, $L_x = 1.72$ nm; and $L_y = 1.13$ nm for model V3. Equilibrium configurations of supercells of the models V1, V2, and V3 are shown in Figure 1. This figure also shows expanded fragments of each of the topological models obtained by multiple translation of supercells in the direction of the X and Y axes.

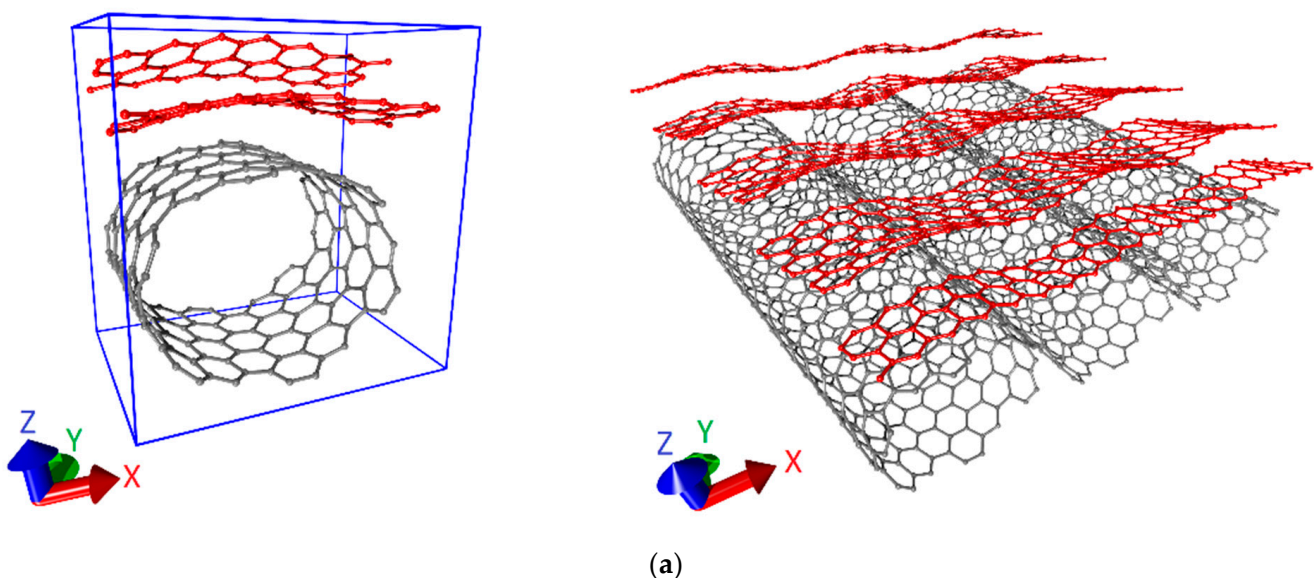


Figure 1. Cont.

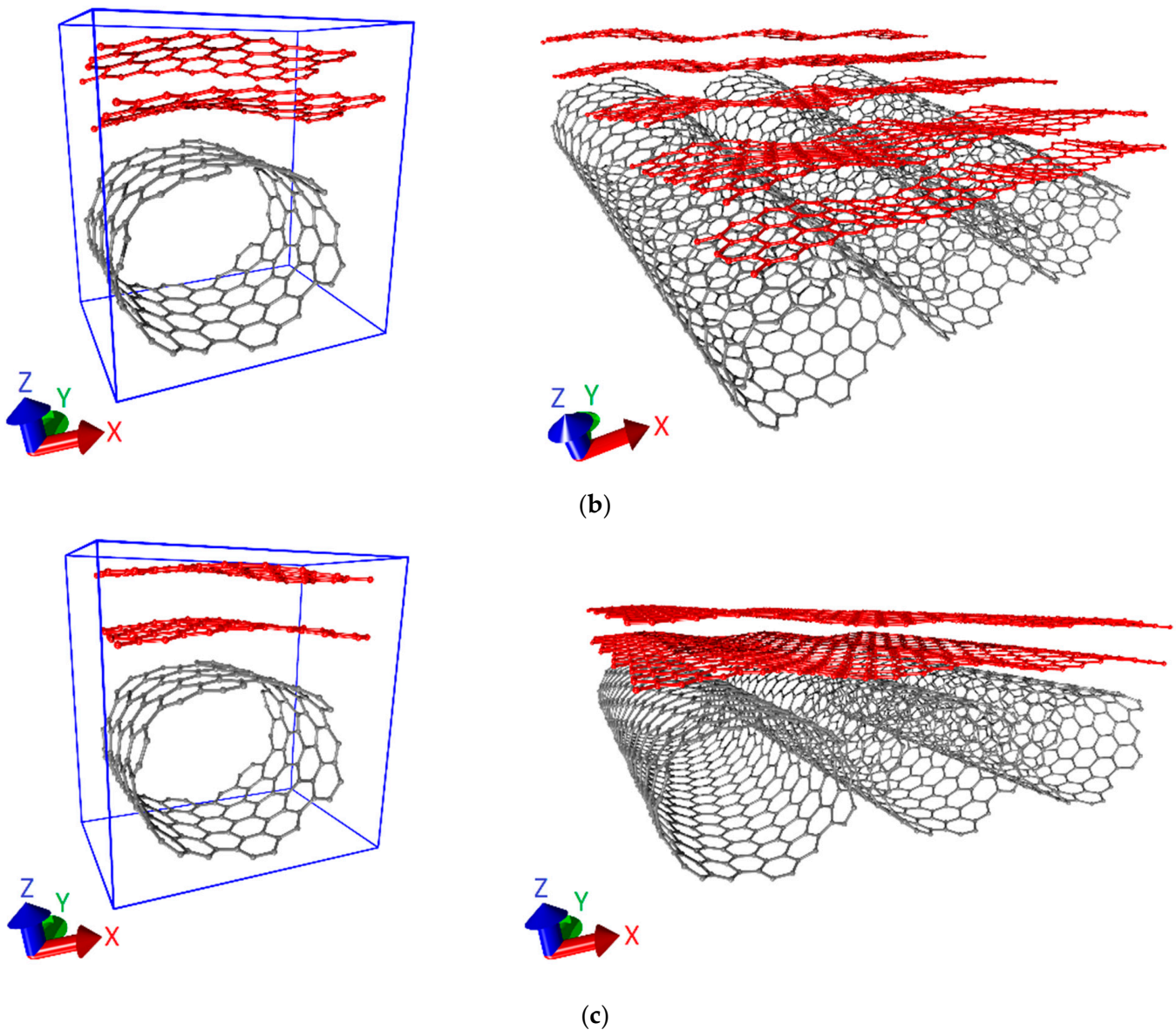


Figure 1. Supercells (left) and extended fragments (right) of composite films formed by bilayer graphene and SWCNTs (12,6): (a) model V1; (b) model V2; (c) model V3. The blue box represents the periodic box.

As noted in the introduction, our main task was to study the optical properties of bilayer graphene-SWCNT (12,6) composite films with an island topology. The analysis of optical properties was carried out on the basis of the results of calculating the complex optical surface conductivity tensor σ in the wavelength range of 0.02–2 μm , i.e., in the UV-, visible, and near-IR ranges. Since the object under study is a composite bilayer graphene-SWCNT structure, it was interesting to establish what contribution each of the carbon materials separately makes to the formation of the spectral profile of optical conductivity. Figures 2–4 show the profiles of the real part of the diagonal elements of the optical surface conductivity tensor for the considered topological models V1, V2, and V3, respectively. They are the graphs of the real part of the complex conductivity σ that were chosen for display, since it determines the optical transitions and absorption of the energy of electromagnetic radiation. Two cases of electromagnetic radiation polarization are considered: along the X axis (along the graphene bilayer) and along the Y axis (along the nanotube axis). The presented graphs demonstrate that, depending on the direction of

polarization of electromagnetic radiation, bilayer graphene and SWCNTs (12,6) exhibit their optical properties in different ways in the bilayer graphene-SWCNT (12,6) composite film. At the same time, attention is drawn to the similarity in the behavior of the characteristics $\text{Re } \sigma_{xx}$ and $\text{Re } \sigma_{yy}$ between models V1 and V2. For these models, the following regularities in the formation of the optical conductivity profile can be noted. In the case of polarization of the electromagnetic radiation along the X axis, the $\text{Re } \sigma_{xx}$ profile in the region of extreme and middle UV radiation is due to the contribution of SWCNTs (12,6), and in the region of near UV and visible radiation, it is due to the contribution of bilayer graphene. In the region of near IR radiation, the influence of both graphene (in the wavelength range 0.8–1.1 μm) and SWCNT (12,6) (in the wavelength range of 1.1–1.6 μm) is manifested. In the case of radiation polarization along the Y axis, the profile $\text{Re } \sigma_{yy}$ in the region of extreme and near UV radiation, as well as visible radiation, is due to the contribution of SWCNT (12,6); in the region of the mid-UV range, it is due to bilayer graphene. In the region of near IR radiation, the characteristic peak at a wavelength of 0.82 μm is due to the contribution of SWCNTs (12,6), and within the interval 0.9–2 μm , it is due to the contribution of graphene. Thus, it can be said that bilayer graphene and SWCNTs (12,6) change places within the UV and visible ranges during the formation of the optical conductivity profile of the bilayer graphene-SWCNT (12,6) composite, depending on the polarization of electromagnetic radiation.

The patterns of the $\text{Re } \sigma_{xx}$ and $\text{Re } \sigma_{yy}$ profiles of the model V3 differ from those of the models V1 and V2. These differences are especially noticeable when the electromagnetic radiation is polarized along the X axis (along bilayer graphene). In this case, the influence of bilayer graphene is more noticeable in the UV range, and the $\text{Re } \sigma_{xx}$ profile completely repeats the law of change of $\text{Re } \sigma_{xx}$ for SWCNT (12,6) in the ranges of visible and IR radiation. Multiple optical conductivity peaks in the visible range on the $\text{Re } \sigma_{xx}$ graphs of models V1 and V2 are absent in the case of model V3. When radiation is polarized along the Y axis, the $\text{Re } \sigma_{yy}$ graphs of all three models of graphene-SWCNT (12,6) composite films have a certain similarity in the region of near UV, visible, and near IR radiation. The difference of the model V3 in this case only lies in the appearance of an additional conductivity peak in the extremal UV region at a wavelength of 0.08 μm , due to the influence of graphene. The reasons for the above differences in the optical conductivity profiles lie in the topological features of the models V1, V2, and V3. Let us consider them using the extended fragments of atomic structure of graphene-SWCNT (12,6) composite films shown in Figure 1. The atomic structure of extended fragments of composite films of models V1 and V2 consists of many rows of graphene nanoribbons oriented at an angle with respect to the SWCNT (12,6) surface. The atomic structure of an extended fragment of model V3 is not represented by a set of graphene nanoribbons, but by two graphene sheets with linear dimensions that differ little from each other. That is, when the width of the bilayer graphene nanoribbon was four hexagons, the translated fragments of supercells approached along the Y axis at a distance sufficient to form covalent bonds with each other. The nanotube (12,6) in the composition of models V1, V2, and V3 is the same; therefore, when the electromagnetic radiation is polarized along the Y axis, there is a similarity in the graphs of $\text{Re } \sigma_{yy}$ between all models. Therefore, the orientation of the graphene bilayer relative to the SWCNT (12,6) surface is the key factor in determining the spectral profile of the optical surface conductivity of composite films.

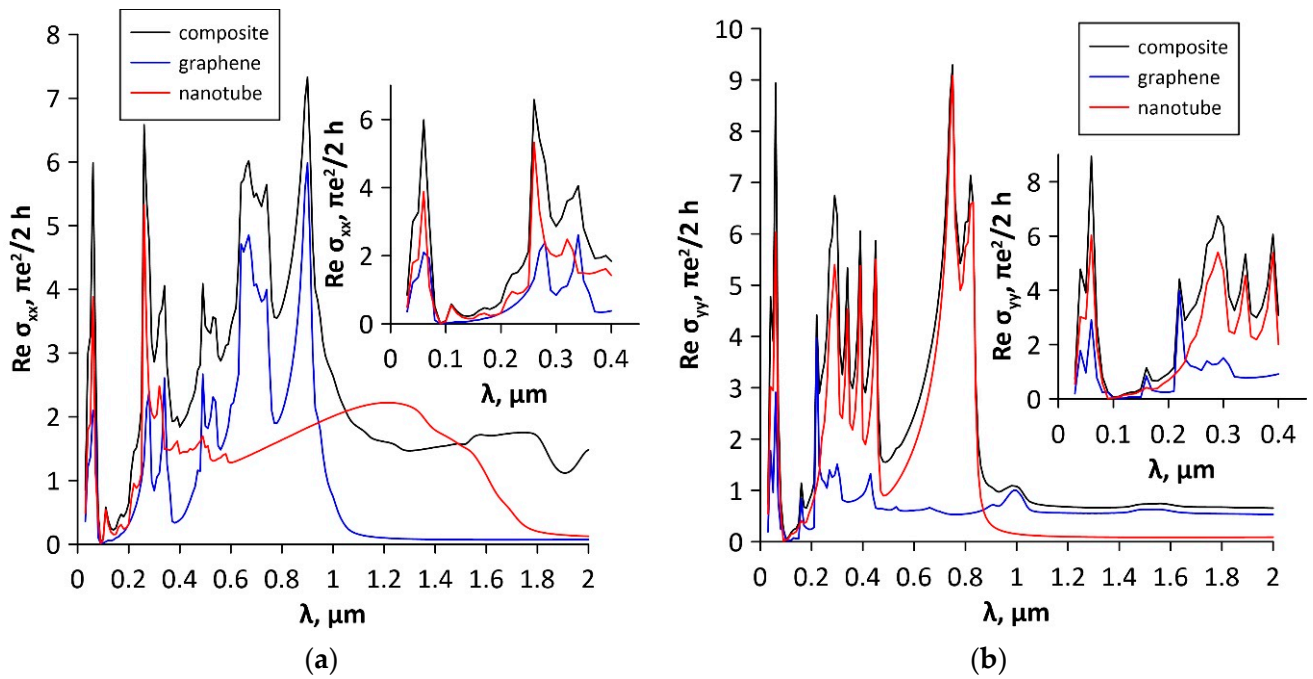


Figure 2. Profiles of the real part of the diagonal elements of the optical surface conductivity tensor for topological model V1 of a graphene-SWCNT (12,6) composite film: (a) with polarization along the X axis; (b) with polarization along the Y axis.

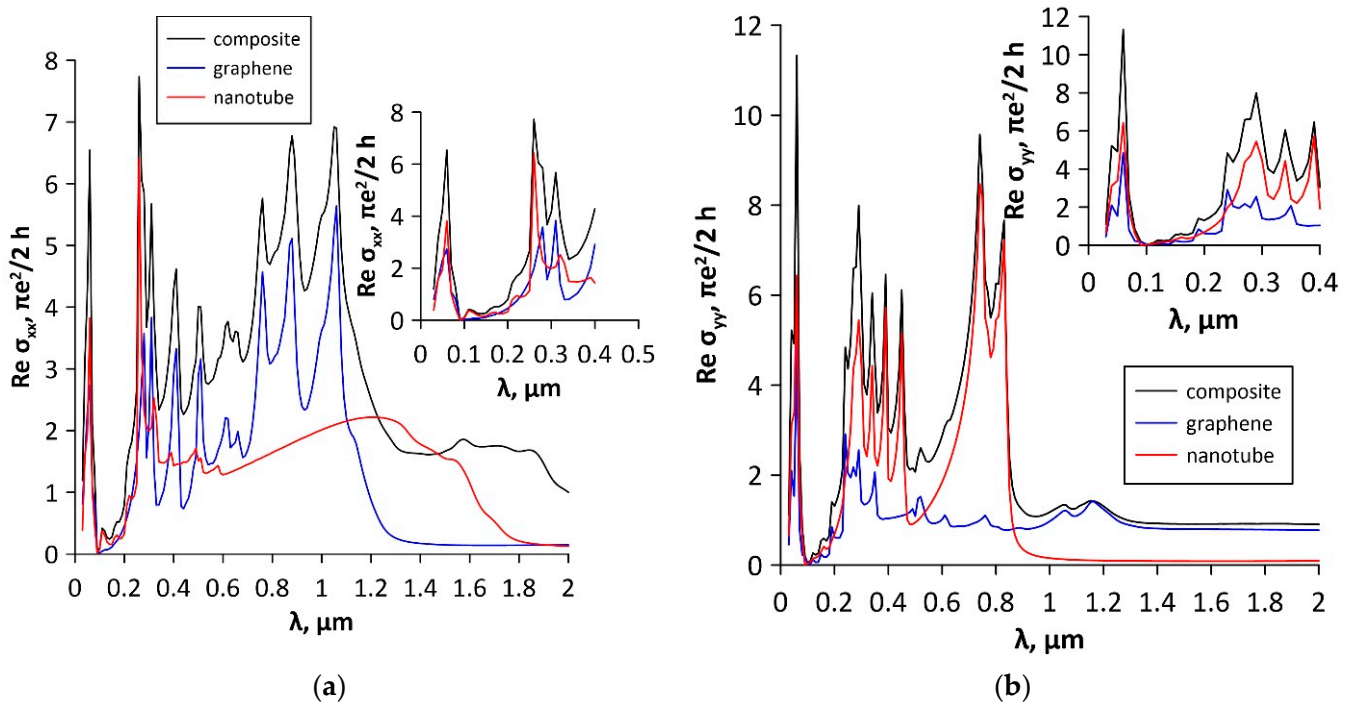


Figure 3. Profiles of the real part of the diagonal elements of the optical surface conductivity tensor for topological model V2 of a graphene-SWCNT (12,6) composite film: (a) with polarization along the X axis; (b) with polarization along the Y axis.

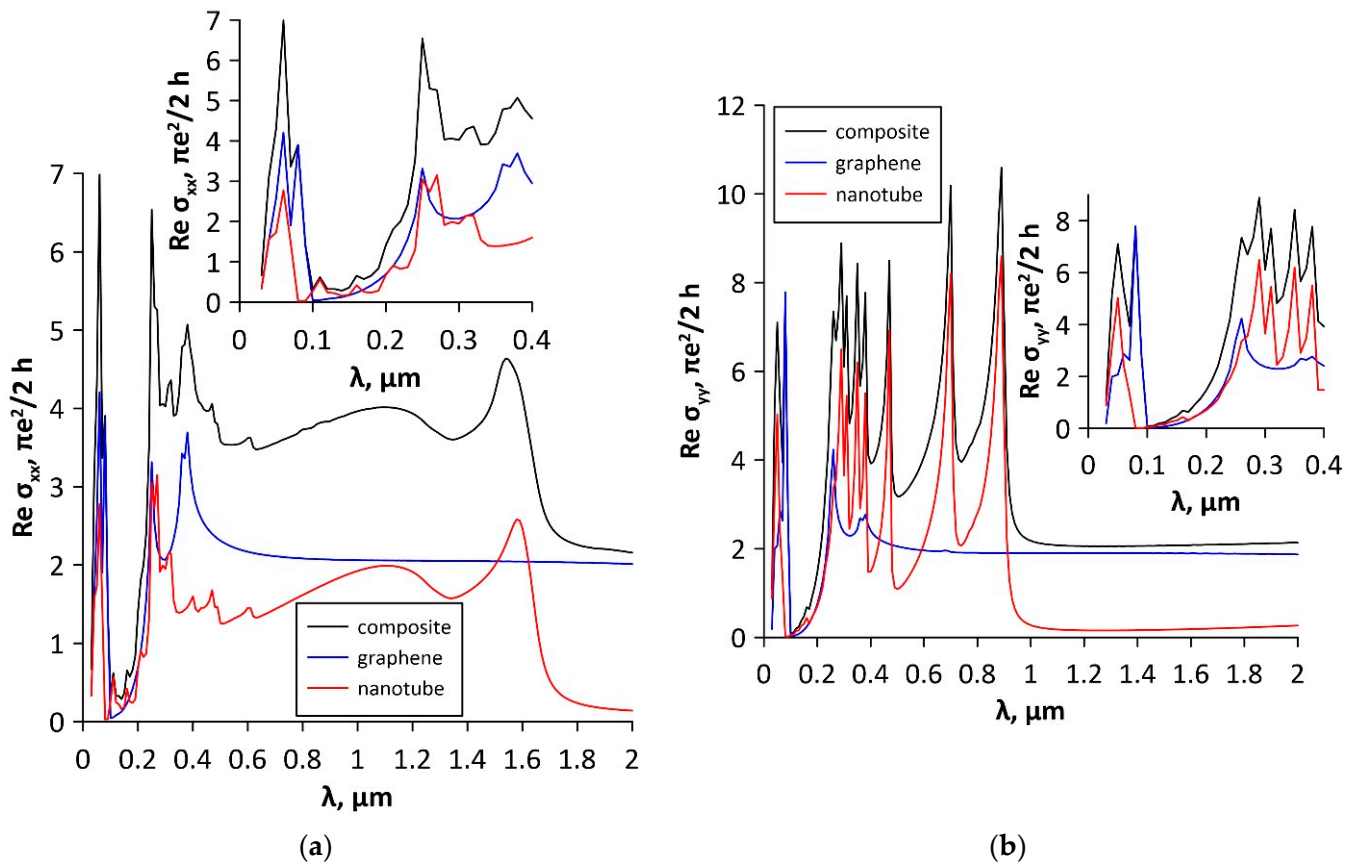


Figure 4. Profiles of the real part of the diagonal elements of the optical surface conductivity tensor for topological model V3 of a graphene-SWCNT (12,6) composite film: (a) with polarization along the X axis; (b) with polarization along the Y axis.

The regularities established by us for the influence of AB-stacked bilayer graphene and SWCNTs (12,6) on the formation of the optical properties of bilayer graphene-SWCNTs (12,6) composite films are indirectly confirmed by the results of other authors. The decisive contribution of AB-stacked bilayer graphene to the optical conductivity of the bilayer graphene-SWCNT (12,6) composite films in the region of near UV radiation is confirmed by the calculation results of Wang et al. [55]. Using the Kubo formula to estimate the optical conductivity, the authors showed that the AB-stacked bilayer graphene has a conductivity peak at the same wavelength ($\sim 0.34 \mu\text{m}$) as the AB-stacked bilayer graphene in bilayer graphene-SWCNT (12,6) composite film. The decisive role of chiral SWCNTs (12,6) in the formation of the spectral profile of the optical conductivity of bilayer graphene-SWCNT (12,6) composite films in the region of mid-UV radiation is confirmed by the experimental data of Mitin et al. [56]. According to the results of [56], SWCNTs with a diameter in the range of $0.9\text{--}3 \mu\text{m}$ have a conductivity peak in the region of mid-UV radiation. In addition, the peak of the optical conductivity of SWCNTs (12,6) ($\sim 7\text{--}9$ conduction quantum) in the bilayer graphene-SWCNT (12,6) composite films when electromagnetic radiation is polarized along the axis of the nanotubes is close to the experimentally measured value of the optical conductivity of SWCNTs with a diameter of 1.2 nm ($\sim 7\text{--}8$ conduction quantum) [57].

The next stage of the study was the identification of regularities in the change in the profile of the optical surface conductivity of bilayer graphene-SWCNT (12,6) composite films under the action of tensile deformation. It was important to evaluate how the deformation affects the location of the optical conductivity peaks. Stretching along the X axis was modeled; i.e., along the zigzag edge of the bilayer graphene nanoribbon in the supercell. This variant of application of the tensile force is due to two reasons: (1) the graphene bilayer has the shape of a nanoribbon as part of a supercell; (2) nanotube (12,6)

and bilayer graphene interact through van der Waals forces. During the simulation, the translation vector length L_x of the supercells of the models V1, V2, and V3 was increased by 1% at each deformation step. Then, the atomic structure of supercells was reoptimized in order to find a new energy-stable configuration. Based on the results of the simulations, it was found that the behavior of supercells of models V2 and V3 was similar in the course of stretching: the initially curvilinear graphene bilayer straightens under the action of a load. The graphene layers in the supercell of model V1 also showed a tendency to straighten out as they were stretched. However, when stretched by 9%, the planar configuration of the graphene layers is replaced by a wave-like one; the bilayer graphene-SWCNT (12,6) composite structure passes into a new phase state. The described patterns of behavior of supercells of models V1, V2, and V3 can be traced from Figure 5. For each model, the strength limits of the atomic network are established: the breaking of covalent bonds for models V1 and V2 occurs when stretched by 15%; for model V3, the breaking of covalent bonds occurs when stretched by 12%.

Figure 6 shows the $\text{Re } \sigma_{xx}$ graphs of the supercells of the topological models V1, V2, and V3 under stretching by various percentages. The above-mentioned changes in the atomic structure of supercells during axial stretching are also reflected in the behavior of the optical conductivity of models V1, V2, and V3. In particular, the transition to a new phase state of the supercell of model V1 upon stretching by 9% leads to the complete disappearance of high-intensity conduction peaks within the visible radiation range and at the very beginning of the near-IR radiation range. Before the onset of the phase transition, only the intensity of the conduction peaks in the UV, visible, and near-IR radiation ranges changed by 1–8% under stretching. For the model V2, the height of the conductivity peaks changes with increasing stretching, and it increases at small strains and decreases at large strains in all considered wavelength ranges. For the model V3, the height of the peaks in the UV range only decreases, while in the near IR range it increases with increasing deformation. For models V1 and V2, one can also note the shift of the conductivity peaks in the region of extreme UV radiation along the wavelength to the right. For the model V3, the shift of the conductivity peaks to the right along the wavelength is observed not only in the region of extreme UV radiation, but also in the region of visible radiation.

The regularities of changes in the optical conductivity of bilayer graphene-SWCNT (12,6) composite films established by us under uniaxial stretching were compared with the results of calculations of the optical conductivity of monolayer graphene under uniaxial stretching [58]. The comparison showed that both in our study and in the study of Pereira et al., performed within the framework of the Kubo-Greenwood formalism, the optical conductivity remains roughly constant in wavelength for the visible and IR radiation ranges, but its magnitude depends on the value of the deformation. In addition, similarity is also observed in the behavior of optical conductivity in the UV range between the bilayer graphene-SWCNT (12,6) composite films and monolayer graphene: with increasing stretch, the conductivity peaks shift along the wavelength to the right.

In general, analyzing the dependencies of $\text{Re } \sigma_{xx}$ in Figure 6, it can be concluded that the model V2 is the least sensitive to axial stretching. This model also demonstrates the highest tensile strength among the considered models. It can be assumed that, along with the orientation of the graphene bilayer with respect to the SWCNT surface, important topological parameters in determining the optical conductivity of graphene-SWCNT (12,6) composite films with island topology are the width of the graphene nanoribbon and the shift of the graphene layers in the composition supercells.

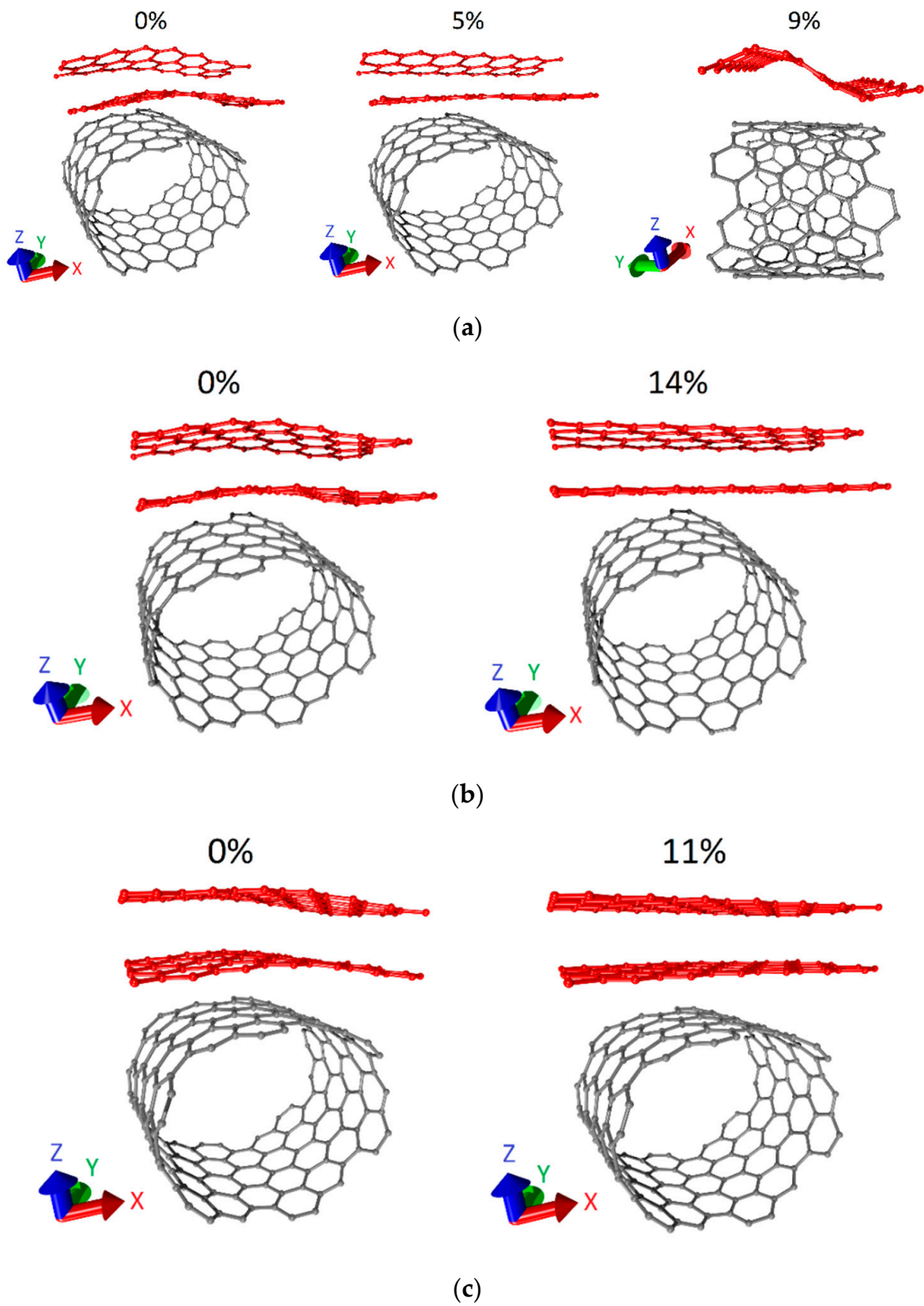


Figure 5. Changes in the atomic structure of supercells of bilayer graphene-SWCNTs (12,6) composite films upon axial tensile: (a) model V1; (b) model V2; (c) model V3.

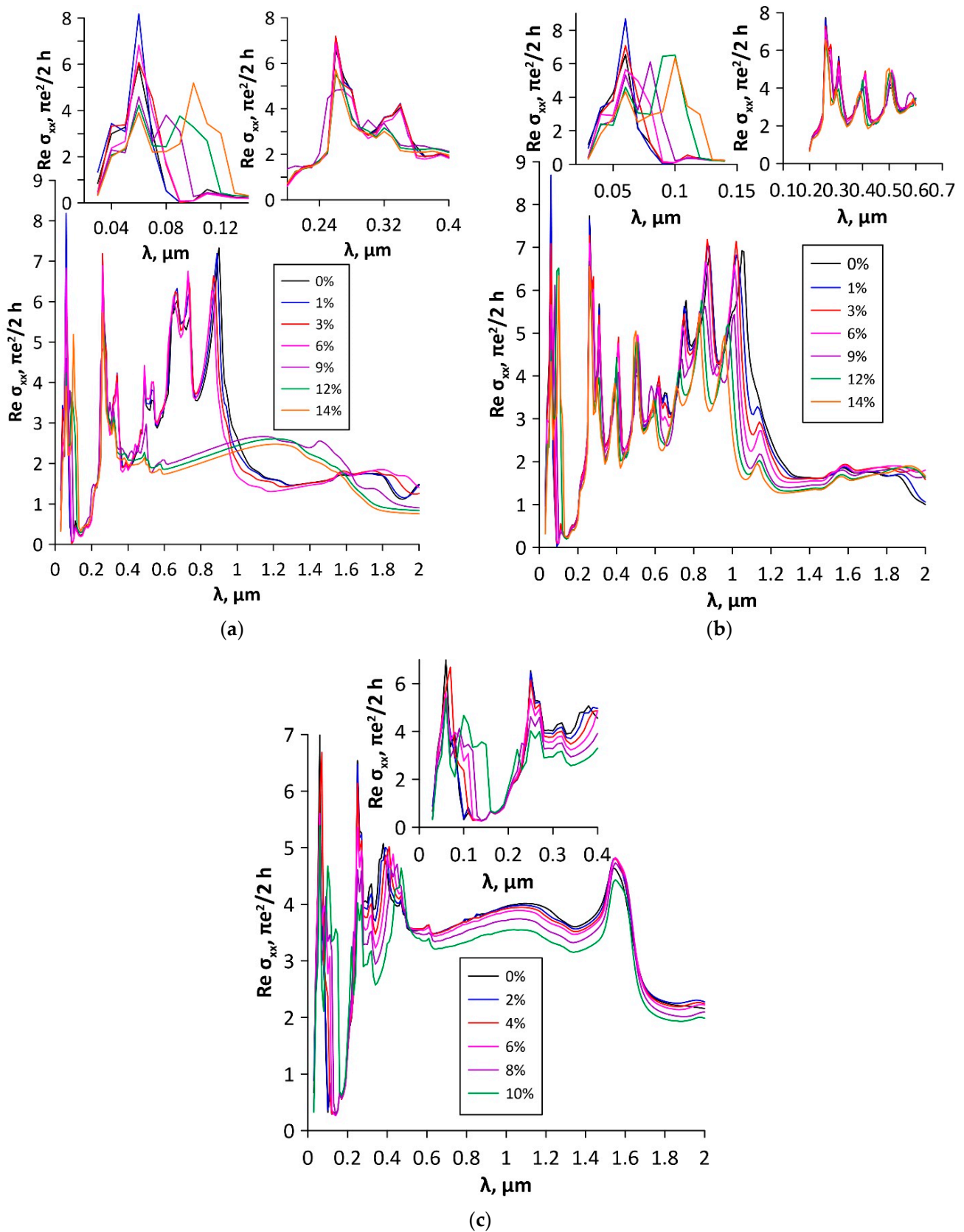


Figure 6. Profiles of the real part of the diagonal element σ_{xx} of the optical surface conductivity tensor of a graphene-SWCNT (12,6) composite film upon axial tensile: (a) model V1; (b) model V2; (c) model V3.

4. Conclusions

Thus, a predictive study of the optical properties of graphene-SWCNT composite films with an island-type topology, including in the presence of axial tensile deformation, was carried out in the article. For three topological models of composite 2D structures formed by bilayer graphene and SWCNTs (12,6), regularities in the formation of the optical surface conductivity profile in the UV, visible, and near-IR ranges were revealed. Quantum calculations shows that bilayer graphene and SWCNTs (12,6) change roles within the UV and visible ranges during the formation of the optical surface conductivity profile of the graphene-SWCNT (12,6) composite, depending on the polarization of electromagnetic radiation. Regularities in the change in the real part of the optical surface conductivity profile of each model under axial stretching are revealed. For model V1 with a bilayer graphene nanoribbon width of two hexagons, there is a complete disappearance of high-intensity conduction peaks within the visible range and the near-IR range when stretched by 9%. This is due to the transition of the composite structure to a new phase state, in which graphene nanoribbons take on a wave-like shape. For models V2 and V3, as the stretching increases, the height of the conductivity peaks changes in all considered wavelength ranges, as well as their shift on the wavelength scale to the right. The least sensitive to axial stretching is the model V2, with a bilayer graphene nanoribbon width of three hexagons in the supercell. It can be assumed that graphene-SWCNT (12,6) composite films with island topology are promising materials for photodetectors in the UV-visible and near-IR ranges.

Author Contributions: Conceptualization, O.E.G. and M.M.S.; methodology, O.E.G.; funding acquisition, M.M.S.; investigation, O.E.G., P.V.B. and M.M.S.; writing—original draft preparation, P.V.B.; writing—review and editing, O.E.G. and M.M.S. All authors have read and agreed to the published version of the manuscript.

Funding: The research was funded by the Council on grants of the President of the Russian Federation (project No. MK-2289.2021.1.2).

Data Availability Statement: The data that support the findings of this study are available on request from the corresponding author.

Conflicts of Interest: The authors declare no conflict of interest.

References

1. Xu, T.; Yang, D.; Fan, Z.; Li, X.; Liu, Y.; Guo, C.; Zhang, M.; Yu, Z.-Z. Reduced graphene oxide/carbon nanotube hybrid fibers with narrowly distributed mesopores for flexible supercapacitors with high volumetric capacitances and satisfactory durability. *Carbon* **2019**, *152*, 134–143. [[CrossRef](#)]
2. Sagade, A.A.; Nyayadhish, A. A carbon nanotube–graphene nanoribbon seamless junction transistor. *Nanoscale Adv.* **2020**, *2*, 659–663. [[CrossRef](#)]
3. Yang, Y.; Yang, X.; Liang, L.; Gao, Y.; Cheng, H.; Li, X.; Zou, M.; Ma, R.; Yuan, Q.; Duan, X. Large-area graphene-nanomesh/carbon-nanotube hybrid membranes for ionic and molecular nanofiltration. *Science* **2019**, *364*, 1057–1062. [[CrossRef](#)]
4. Gao, M.; Huang, Z.L.; Zeng, B.; Pan, T.S.; Zhang, Y.; Peng, H.B.; Lin, Y. Carbon nanotube-graphene junctions studied by impedance spectra. *Appl. Phys. Lett.* **2015**, *106*, 051601. [[CrossRef](#)]
5. Gbaguidi, A.; Namilae, S.; Kim, D. Synergy effect in hybrid nanocomposites based on carbon nanotubes and graphene nanoplatelets. *Nanotechnology* **2020**, *31*, 255704. [[CrossRef](#)] [[PubMed](#)]
6. Xia, K.; Zhan, H.; Gu, Y. Graphene and Carbon Nanotube Hybrid Structure: A Review. *Procedia IUTAM* **2017**, *21*, 94–101. [[CrossRef](#)]
7. Dang, V.T.; Nguyen, D.D.; Cao, T.T.; Le, P.H.; Tran, D.L.; Phan, N.M.; Nguyen, V.C. Recent trends in preparation and application of carbon nanotube–graphene hybrid thin films. *Adv. Nat. Sci. Nanosci. Nanotechnol.* **2016**, *7*, 033002. [[CrossRef](#)]
8. Du, W.; Ahmed, Z.; Wang, Q.; Yu, C.; Feng, Z.; Li, G.; Zhang, M.; Zhou, C.; Senegor, R.; Yang, C.Y. Structures, properties, and applications of CNT-graphene heterostructures. *2D Mater.* **2019**, *6*, 042005. [[CrossRef](#)]
9. Zhang, J.; Chen, Z.; Xu, X.; Liao, W.; Yan, L. A simple and efficient approach to fabricate graphene/CNT hybrid transparent conductive films. *RSC Adv.* **2017**, *7*, 52555–52560. [[CrossRef](#)]
10. Li, L.; Li, H.; Guo, Y.; Yang, L.; Fang, Y. Direct synthesis of graphene/carbon nanotube hybrid films from multiwalled carbon nanotubes on copper. *Carbon* **2017**, *118*, 675–679. [[CrossRef](#)]
11. Lv, R.; Cruz-Silva, E.; Terrones, M. Building Complex Hybrid Carbon Architectures by Covalent Interconnections: Graphene-Nanotube Hybrids and More. *ACS Nano* **2014**, *8*, 4061–4069. [[CrossRef](#)] [[PubMed](#)]

12. Yousefi, K. Graphene-Carbon Nanotube Hybrids: Synthesis and Application. *J. Environ. Treat. Tech.* **2021**, *9*, 224.
13. Kim, S.H.; Song, W.; Jung, M.W.; Kang, M.A.; Kim, K.; Chang, S.J.; Lee, S.S.; Lim, J.; Hwang, J.; Myung, S.; et al. Carbon Nanotube and Graphene Hybrid Thin Film for Transparent Electrodes and Field Effect Transistors. *Adv. Mater.* **2014**, *26*, 4247–4252. [[CrossRef](#)] [[PubMed](#)]
14. Kholmanov, I.N.; Magnuson, C.W.; Piner, R.; Kim, J.Y.; Aliev, A.E.; Tan, C.; Kim, T.Y.; Zakhidov, A.A.; Sberveglieri, G.; Baughman, R.H.; et al. Optical, electrical, and electromechanical properties of hybrid graphene/carbon nanotube films. *Adv. Mater.* **2015**, *27*, 3053–3059. [[CrossRef](#)]
15. Nguyen, D.D.; Tiwari, R.N.; Matsuoka, Y.; Hashimoto, G.; Rokuta, E.; Chen, Y.Z.; Chueh, Y.L.; Yoshimura, M. Low Vacuum Annealing of Cellulose Acetate on Nickel Towards Transparent Conductive CNT–Graphene Hybrid Films. *ACS Appl. Mater. Interfaces.* **2014**, *6*, 9071–9077. [[CrossRef](#)]
16. Zhou, W.; Bai, X.; Wang, E.; Xie, S. Synthesis, Structure, and Properties of Single-Walled Carbon Nanotubes. *Adv. Mater.* **2009**, *21*, 4565–4583. [[CrossRef](#)]
17. Liu, Y.; Wang, F.; Wang, X.; Wang, X.; Flahaut, E.; Liu, X.; Li, Y.; Wang, X.; Xu, Y.; Shi, Y.; et al. Planar carbon nanotube–graphene hybrid films for high-performance broadband photodetectors. *Nat. Commun.* **2015**, *6*, 8589. [[CrossRef](#)]
18. Lin, X.; Liu, P.; Wei, Y.; Li, Q.; Wang, J.; Wu, Y.; Feng, C.; Zhang, L.; Fan, S.; Jiang, K. Development of an ultrathin film comprised of a graphene membrane and carbon nanotube vein support. *Nat. Commun.* **2013**, *4*, 2920. [[CrossRef](#)]
19. Yan, Z.; Peng, Z.; Casillas, G.; Lin, J.; Xiang, C.; Zhou, H.; Yang, Y.; Ruan, G.; Raji, A.R.O.; Samuel, E.L.G.; et al. Rebar graphene. *ACS Nano* **2014**, *8*, 5061–5068. [[CrossRef](#)]
20. Gan, X.; Lv, R.; Bai, J.; Zhang, Z.; Wei, J.; Huang, Z.H.; Zhu, H.; Kang, F.; Terrones, M. Efficient photovoltaic conversion of graphene–carbon nanotube hybrid films grown from solid precursors. *2D Mater.* **2015**, *2*, 034003. [[CrossRef](#)]
21. Li, X.L.; Sha, J.W.; Lee, S.K.; Li, Y.L.; Ji, Y.S.; Zhao, Y.J.; Tour, J.M. Rivet graphene. *ACS Nano* **2016**, *10*, 7307–7313. [[CrossRef](#)] [[PubMed](#)]
22. Kim, H.; Kim, J.; Jeong, H.S.; Kim, H.; Lee, H.; Ha, J.M.; Choi, S.M.; Kim, T.H.; Nah, Y.C.; Shin, T.J.; et al. Spontaneous hybrids of graphene and carbon nanotube arrays at the liquid-gas interface for Li-ion battery anodes. *Chem. Commun.* **2018**, *54*, 5229–5232. [[CrossRef](#)]
23. Kumar, P.; Woon, K.L.; Wong, W.S.; Saheed, M.S.M.; Burhanudin, Z.A. Hybrid film of single-layer graphene and carbon nanotube as transparent conductive electrode for organic light emitting diode. *Synth. Met.* **2019**, *257*, 116186. [[CrossRef](#)]
24. Cai, B.; Yin, H.; Huo, T.; Ma, J.; Di, Z.; Li, M.; Hu, N.; Yang, Z.; Zhang, Y.; Su, Y. Semiconducting single-walled carbon nanotube/graphene van der Waals junctions for highly sensitive all-carbon hybrid humidity sensors. *J. Mater. Chem. C* **2020**, *8*, 3386–3394. [[CrossRef](#)]
25. Shi, E.; Li, H.; Yang, L.; Hou, J.; Li, Y.; Li, L.; Cao, A.; Fang, Y. Carbon nanotube network embroidered graphene films for monolithic all-carbon electronics. *Adv. Mater.* **2015**, *27*, 682–688. [[CrossRef](#)] [[PubMed](#)]
26. Hong, X.; Shi, W.; Zheng, H.; Liang, D. Effective carbon nanotubes/graphene hybrid films for electron field emission application. *Vacuum* **2019**, *169*, 108917. [[CrossRef](#)]
27. Liu, Y.; Liu, Y.; Qin, S.; Xu, Y.; Zhang, R.; Wang, F. Graphene-carbon nanotube hybrid films for high-performance flexible photodetectors. *Nano Res.* **2017**, *10*, 1880–1887. [[CrossRef](#)]
28. Maarouf, A.; Kasry, A.; Chandra, B.; Martyna, G. A graphene–carbon nanotube hybrid material for photovoltaic applications. *Carbon* **2015**, *102*, 74–80. [[CrossRef](#)]
29. Cao, J.; Zou, Y.; Gong, X.; Qian, R.; An, Z. Scalable Production of Graphene/Semiconducting Single-Wall Carbon Nanotube Film Schottky Broadband Photodiode Array with Enhanced Photoresponse. *Appl. Sci.* **2018**, *8*, 2369. [[CrossRef](#)]
30. Wang, Z.; Li, J.; Yuan, K. Molecular dynamics simulation of thermal boundary conductance between horizontally aligned carbon nanotube and graphene. *Int. J. Therm. Sci.* **2018**, *132*, 589–596. [[CrossRef](#)]
31. Lepak-Kuc, S.; Milowska, K.Z.; Boncel, S.; Szybowicz, M.; Dychalska, A.; Jozwik, I.; Koziol, K.K.; Jakubowska, M.; Lekawa-Raus, A. Highly Conductive Doped Hybrid Carbon Nanotube–Graphene Wires. *ACS Appl. Mater. Interfaces* **2019**, *11*, 33207–33220. [[CrossRef](#)] [[PubMed](#)]
32. Srivastava, J.; Gaur, A. Tight-binding investigation of the structural and vibrational properties of graphene–single wall carbon nanotube junctions. *Nanoscale Adv.* **2021**, *3*, 2030–2038. [[CrossRef](#)]
33. Valeev, B.Y.; Toksumakov, A.N.; Kvashnin, D.G.; Chernozatonskii, L.A. Theoretical Study of the Electronic and Transport Properties of Lateral 2D–1D–2D Graphene–CNT–Graphene Structures. *JETP Lett.* **2022**, *115*, 93–97. [[CrossRef](#)]
34. Srivastava, J.; Gaur, A. A tight-binding study of the electron transport through single-walled carbon nanotube-graphene hybrid nanostructures. *J. Chem. Phys.* **2021**, *155*, 244104. [[CrossRef](#)]
35. Kolosov, D.A.; Mitrofanov, V.V.; Slepchenkov, M.M.; Glukhova, O.E. Thin Graphene–Nanotube Films for Electronic and Photovoltaic Devices: DFTB Modeling. *Membranes* **2020**, *10*, 341. [[CrossRef](#)] [[PubMed](#)]
36. Felix, A.B.; Pacheco, M.; Orellana, P.; Latgé, A. Vertical and In-Plane Electronic Transport of Graphene Nanoribbon/Nanotube Heterostructures. *Nanomaterials* **2022**, *12*, 3475. [[CrossRef](#)]
37. Wei, L.; Zhang, L. Atomic Simulations of (8,0)CNT-Graphene by SCC-DFTB Algorithm. *Nanomaterials* **2022**, *12*, 1361. [[CrossRef](#)] [[PubMed](#)]
38. Zhang, S.; Kang, L.; Wang, X.; Tong, L.; Yang, L.; Wang, Z.; Qi, K.; Deng, S.; Li, Q.; Bai, X.; et al. Arrays of horizontal carbon nanotubes of controlled chirality grown using designed catalysts. *Nature* **2017**, *543*, 234–238. [[CrossRef](#)]

39. Elstner, M.; Seifert, G. Density functional tight binding. *Phil. Trans. R. Soc. A* **2014**, *372*, 20120483. [[CrossRef](#)] [[PubMed](#)]
40. Mulliken, R.S. Electronic Population Analysis on LCAO–MO Molecular Wave Functions I. *J. Chem. Phys.* **1955**, *23*, 1833. [[CrossRef](#)]
41. Porezag, D.; Pederson, M.R.; Frauenheim, T.; Köhler, T. Structure, stability, and vibrational properties of polymerized C60. *Phys. Rev. B* **1995**, *52*, 14963–14970. [[CrossRef](#)]
42. Porezag, D.; Frauenheim, T.; Köhler, T.; Seifert, G.; Kaschner, R. Construction of tight-binding-like potentials on the basis of density-functional theory: Application to carbon. *Phys. Rev. B* **1995**, *51*, 12947–12957. [[CrossRef](#)]
43. Elstner, M.; Porezag, D.V.; Jungnickel, G.; Elsner, J.W.; Haugk, M.; Frauenheim, T.; Suhai, S.; Seifert, G. Self-consistent-charge density-functional tight-binding method for simulations of complex materials properties. *Phys. Rev. B* **1998**, *58*, 7260–7268. [[CrossRef](#)]
44. Skowron, S.T.; Lebedeva, I.V.; Popov, A.M.; Bichoutskaia, E. Energetics of atomic scale structure changes in graphene. *Chem. Soc. Rev.* **2015**, *44*, 3143–3176. [[CrossRef](#)]
45. Niu, J.; Li, M.; Choi, W.; Dai, L.; Xia, Z. Growth of junctions in 3D carbon nanotube-graphene nanostructures: A quantum mechanical molecular dynamic study. *Carbon* **2014**, *67*, 627–634. [[CrossRef](#)]
46. Fülep, D.; Zsoldos, I.; László, I. Topological and Energetic Conditions for Lithographic Production of Carbon Nanotubes from Graphene. *J. Nanomater.* **2015**, *2015*, 379563. [[CrossRef](#)]
47. Jung, G.S.; Irle, S.; Sumpter, B.G. Dynamic aspects of graphene deformation and fracture from approximate density functional theory. *Carbon* **2022**, *190*, 183–193. [[CrossRef](#)]
48. Glukhova, O.E.; Nefedov, I.S.; Shalin, A.S.; Slepchenkov, M.M. New 2D graphene hybrid composites as an effective base element of optical nanodevices. *Beilstein J. Nanotechnol.* **2018**, *9*, 1321–1327. [[CrossRef](#)] [[PubMed](#)]
49. Slepchenkov, M.M.; Shmygin, D.S.; Zhang, G.; Glukhova, O.E. Controlling the electronic properties of 2D/3D pillared graphene and glass-like carbon via metal atom doping. *Nanoscale* **2019**, *11*, 16414–16427. [[CrossRef](#)] [[PubMed](#)]
50. Slepchenkov, M.M.; Barkov, P.V.; Glukhova, O.E. Hybrid Films Based on Bilayer Graphene and Single-Walled Carbon Nanotubes: Simulation of Atomic Structure and Study of Electrically Conductive Properties. *Nanomaterials* **2021**, *11*, 1934. [[CrossRef](#)]
51. Marder, M. *Condensed Matter Physics*, 2nd ed.; John Wiley & Sons: New Jersey, NJ, USA, 2010; pp. 623–631.
52. Calderín, L.; Karasiev, V.V.; Trickey, S.B. Kubo–Greenwood electrical conductivity formulation and implementation for projector augmented wave datasets. *Comput. Phys. Commun.* **2017**, *221*, 118–142. [[CrossRef](#)]
53. Pedersen, T.G.; Pedersen, K.; Kriestensen, T.B. Optical matrix elements in tight-binding calculations. *Phys. Rev. B* **2001**, *63*, 201101. [[CrossRef](#)]
54. Allen, P.B. Electron transport. In *Conceptual Foundations of Materials*, 2nd ed.; Louie, S.G., Cohen, M.L., Eds.; Elsevier Science: Amsterdam, The Netherlands, 2006; Volume 2, pp. 172–175.
55. Wang, Y.; Ni, Z.; Liu, L.; Liu, Y.; Cong, C.; Yu, T.; Wang, X.; Shen, D.; Shen, Z. Stacking-dependent optical conductivity of bilayer graphene. *ACS Nano* **2010**, *4*, 4074–4080. [[CrossRef](#)]
56. Mitin, D.; Vorobyev, A.; Pavlov, A.; Berdnikov, Y.; Mozharov, A.; Mikhailovskii, V.; Ramirez, J.A.B.; Krasnikov, D.V.; Kopylova, D.S.; Kirilenko, D.A.; et al. Tuning the Optical Properties and Conductivity of Bundles in Networks of Single-Walled Carbon Nanotubes. *J. Phys. Chem. Lett.* **2022**, *13*, 8775–8782. [[CrossRef](#)]
57. Joh, D.Y.; Kinder, J.; Herman, L.H.; Ju, S.Y.; Segal, M.A.; Johnson, J.N.; Chan, G.K.; Park, J. Single-walled carbon nanotubes as excitonic optical wires. *Nat. Nanotechnol.* **2011**, *6*, 51–56. [[CrossRef](#)]
58. Pereira, V.M.; Ribeiro, R.M.; Peres, N.M.R.; Castro Neto, A.H. Optical properties of strained graphene. *Europhys. Lett.* **2010**, *92*, 67001. [[CrossRef](#)]

Disclaimer/Publisher’s Note: The statements, opinions and data contained in all publications are solely those of the individual author(s) and contributor(s) and not of MDPI and/or the editor(s). MDPI and/or the editor(s) disclaim responsibility for any injury to people or property resulting from any ideas, methods, instructions or products referred to in the content.